University of Baghdad
College of Engineering
JE
JOURNAL OF ENGINEERING

Journal of Engineering

journal homepage: www.jcoeng.edu.iq

Volume 31 Number 10 October 2025

Study of Heat Generation and Power Losses in MultiCrystalline Silicon Photovoltaic Solar Module

Hassanein Saady Hussein *, Adawiya Ali Hamzah

Department of Energy Engineering, College of Engineering, University of Baghdad, Baghdad, Iraq

ABSTRACT

A photovoltaic modules convert only a fraction of incident solar energy into electricity, with the remainder dissipated as heat through various loss mechanisms. This study makes an attempt to quantify the recoverable thermal energy from multicrystalline silicon photovoltaic modules under varying irradiance conditions for arid climates. Experimental measurements were conducted over six months in Baghdad, Iraq. Data were filtered to maintain 25°C module temperature across four irradiance levels (250, 500, 750, 1000 W/m^2). Results demonstrate thermal losses increasing from 10.33% to 19.02% with rising irradiance, while recoverable thermal energy fraction (ξ_u) ranges from 29.72% to 35.06%. Module efficiency decreased from 18.1% at 500 W/m^2 to 16.7% at 1000 W/m^2, reflecting thermal loss dominance over optical gains. Spectral analysis revealed uniform distribution of recoverable thermal energy across the solar spectrum rather than infrared concentration. The quantified thermal losses provide fundamental data for hybrid photovoltaic-thermal (PV/T) system development optimized for high-irradiance arid conditions, supporting renewable energy advancement where abundant solar resources enable combined electrical and thermal harvesting.

Keywords: Multicrystalline silicon, Thermal losses, Quantum efficiency, Hybrid photovoltaic-thermal systems, Solar irradiance, Arid climate.

1. INTRODUCTION

Photovoltaic technology is among the most promising solutions for sustainable energy, yet commercial silicon solar modules typically convert only 15-22% of incident solar energy into electricity under standard conditions **(Richter et al., 2013)**. The remaining energy is dissipated through various loss mechanisms, predominantly as heat, representing a significant untapped energy resource. Solar module performance is the main factor in converting photovoltaic power into electrical power, with energy conversion being a function of temperature. As temperature rises, the rate of reverse saturation currents increases within the solar panel, affecting overall efficiency. The band gap of semiconductor

*Corresponding author
Peer review under the responsibility of University of Baghdad.
https://doi.org/10.31026/j.eng.2025.10.04

Article received: 05/04/2025
Article revised: 31/08/2025
Article accepted: 08/09/2025
Article published: 01/10/2025

materials, which significantly affects photon absorption in solar cells, varies notably with temperature changes **(Asif et al., 2023)**. When the operating temperature of a solar module increases, the energy threshold for photon absorption can shift, leading to a decline in the number of photons effectively absorbed. Materials characterized by narrower band gaps are capable of capturing lower-energy photons; however, this often results in increased thermal energy losses. Maintaining high efficiency in solar systems requires optimizing material properties and managing heat generation and transfer effectively.

Many studies and developments have been conducted on the effect of temperature on the performance of solar panels, with high or low efficiency **(Barron-Gafford et al., 2016; Bhore et al., 2023)**. In all cases, the profitability of hybrid solar harvesters is limited by the requirement of keeping PV cells at the lowest possible temperature, as their efficiency decreases with temperature at a rate depending on the specific PV material. This is a very well-known hurdle in the making of effective hybrid solar cells, as reported in previous works **(Narducci and Lorenzi, 2016)**. **(Sun et al., 2022)** utilized theoretical modeling to demonstrate that large-scale solar power plants can contribute to localized temperature increases. **(Arifin et al., 2020)** investigated the properties of heat sinks for solar panels and their use to increase efficiency, including the creation of fins to reduce temperatures. Similarly, **(Mesquita et al., 2019)** explored how temperature fluctuations affect fourth-generation solar modules, emphasizing the operational difficulties related to maintaining thermal stability. **(Wei et al., 2021)** analyzed thermal losses arising from various system components, including inverters, charge controllers, and electrical wiring. Supporting this, **(Lipiński et al., 2020; Ma et al., 2021)** highlighted that these components are notable sources of resistive heat loss, which can affect overall system efficiency.

(Aghaei et al., 2020; Nkounga et al., 2021; Aslam et al., 2022) addressed heat generated by these items and examined heat transfer methods, proposing suitable solutions to dissipate it. Since thermal energy contributes to performance degradation in solar systems, evaluating thermal losses under different atmospheric conditions is essential for system optimization. The resistance that occurs in electrical cables and connections causes electrical losses. Higher losses occur in older transformers and the higher the temperature, the shorter the battery life and performance **(Hernandez-Callejo et al., 2019; Sharma et al., 2019; Sarath et al., 2023)**. Improving charge collection efficiency by increasing the forward voltage in the amorphous silicon module to increase its response to the solar spectrum **(Hibberd et al., 2011)**. To eliminate heat and the resulting problems, cooling is used, high-efficiency inverters are selected, very low-resistance wiring is selected, and regular maintenance is performed **(Zhou et al., 2015; Fang et al., 2023)**. While research often targets MPPT and panel modeling **(Hashim and Talib, 2018; Mohammed and Hashim, 2019)**, few studies have experimentally evaluated thermal losses **(Dupre et al., 2015)**.

(Cotfas et al., 2012) emphasized that internal heat generation affects overall performance. They also found a linear relationship between output power and operating temperature. **(Hashim, 2016; Hashim and Abbood, 2016)** developed the four-parameter model using different methods: the slope method and the explicit simplified method. The accuracy of these methods compared to measured data was 5%, 7.9%, and 9.3%, respectively. A hybrid solar energy conversion system combining a concentrator, a photovoltaic cell, and a thermal generator (heat engine or thermoelectric device) was shown to capture both the portion of the spectrum unabsorbed by the semiconductor and the full solar flux at elevated cell temperatures. Modeling across different bandgaps and thermoelectric materials demonstrated that such configurations can achieve practical and efficient overall conversion

efficiencies **(Vorobiev et al., 2005)**. **(Katee et al., 2022)** conducted experimental measurements of current, voltage, and power for two types of solar modules. These data were used to extract the four-parameter model using two different extraction methods. For monocrystalline solar panels, the percentage errors were 5% and 8% for the iterative and simplified explicit methods, respectively, while for the copper indium gallium selenide modules, the errors were 10% and 9%. Additional research on solar module modeling can be found in **(Hashim and Talib, 2018; Kadia et al., 2022)**. **(Richter et al., 2013)** demonstrated how radiative recombination affects the overall performance of silicon solar cells.

Recently, there has been a growing research interest in extracting thermal energy from solar cells as a method to improve overall system efficiency, which requires accurately estimating the amount of recoverable heat and identifying the primary sources of energy loss within the cell. Most previous works emphasize electrical parameters without fully accounting for the spectral and thermal interactions within the PV module. Previous studies have mostly focused on electrical efficiency alone, or sometimes partially discussed quantum efficiency but failed to provide the complete picture. This work attempts to fill this gap by experimentally and theoretically analyzing the heat generation, recombination losses, and the recoverable thermal energy within a multicrystalline silicon module, specifically under Iraqi climatic conditions. This is performed under controlled conditions simulating typical solar irradiance levels. The novelty of this work lies in its integrated assessment of quantum efficiency (both internal and external), thermal power ratio (ξu), and loss components based on the complete solar spectrum. The outcomes provide critical insights for developing hybrid photovoltaic-thermal systems optimized for high-irradiance conditions typical of Iraq and similar arid regions, supporting renewable energy deployment strategies that maximize utilization of abundant solar resources through combined electrical and thermal energy harvesting.

2. EXPERIMENTAL WORK

The experimental investigation was conducted using a multicrystalline silicon photovoltaic module manufactured by Trina Solar (Model: TSM-PD14). The module specifications under Standard Test Conditions (STC: 1000 W/m^2, 25°C, AM 1.5 spectrum) are detailed in **Table 1**. This module represents typical commercial multicrystalline silicon technology with 72 cells arranged in a standard configuration.

Table 1. Panel properties at 1000 (W/m^2) and 25 (˚C).

Area (m^2)	Length (cm)	Width (cm)	V_{oc} (V)	I_{sc} (A)	Peak power (w)	Peak voltage (v)	Peak current (A)	No. of cells	Production data
1.94	196.8	98.4	45.5	9.15	324	37.1	8.73	72	2020
Temperature Coeff. of P_{max}		- 0.41(%/°C)			Temperature Coeff. of V_{oc}	- 0.32(%/°C)	Temperature Coeff. of I_{sc}		0.05(%/°C)

Solar irradiance was measured using a PASCO Wireless Weather Sensor (Model: PS-3209-02) calibrated according to ISO 9060 standards. This pyranometer-based system provides: Measurement range (0-2000 W/m^2), Accuracy (±5% for global horizontal irradiance), Response time (<5 seconds), Spectral range (300-3000 nm), Temperature compensation (-40°C to +70°C), and Data logging frequency (1 measurement per minute). The sensor was positioned in the same plane as the test module and underwent annual calibration against a reference pyranometer traceable to the World Radiometric Reference (WRR).

Electrical characterization was performed using a PROVA 210A Solar Module Analyzer (PROVA Instruments, Taiwan, Serial Number: 11180015) with the following specifications:

- DC voltage range: 0-60 V (Resolution: 0.01 V, Accuracy: ±1%)
- DC current range: 0-61 A (Resolution: 1 mA, Accuracy: ±1%)
- Power calculation accuracy: ±2%
- Measurement time: <2 seconds for complete I-V sweep
- Operating temperature range: 0-50°C
- Data interface: USB connection for direct computer logging
  The analyzer employs electronic load variation from zero to infinity resistance, enabling comprehensive I-V curve generation from short-circuit (0, I_{sc}) to open-circuit (Voc, 0) conditions.

Module surface temperature was monitored using calibrated K-type thermocouples (±0.1°C accuracy) attached to the module back sheet at multiple locations. Ambient temperature was recorded simultaneously using the integrated temperature sensor in the weather monitoring system. All temperature measurements were logged continuously throughout each measurement session.

The experimental campaign was conducted at the Energy Engineering Department, University of Baghdad, Iraq (33.3°N, 44.4°E, and elevation: 34 m). This location represents typical arid continental climate conditions with average annual solar irradiance (2000-2200 kWh/m^2), peak summer temperatures (45-50°C), and low relative humidity (20-40%). The test module was mounted on a fixed-tilt structure oriented due south with a tilt angle of 33° (equal to latitude) to optimize annual energy collection. The mounting system provided adequate ventilation (>10 cm clearance) to minimize thermal boundary layer effects while maintaining representative operating conditions.

3. EXPERIMENTAL PROCEDURE

Experiments were conducted at the University of Baghdad, Iraq (33.3°N, 44.4°E) from September 2024 to February 2025. Measurements were taken between 9:00 AM and 3:00 PM on clear days with cloud cover below 10%. Target irradiance levels were achieved naturally through strategic timing: 250 W/m^2 during early morning (9:00-9:45 AM) and late afternoon (2:15-3:00 PM) in winter months, 500 W/m^2 during mid-morning and mid-afternoon in winter/spring, 750 W/m^2 during late morning in spring/autumn, and 1000 W/m^2 during solar noon in summer under exceptional atmospheric clarity. Module temperature was monitored continuously using four temperature sensors (±0.1°C accuracy) attached to the backsheet. Only measurements where module temperature stabilized at 25°C ± 1°C were retained for analysis to ensure Standard Test Conditions compliance. This filtering process, requiring 5-minute thermal equilibrium and temperature stability below 0.2°C variation, resulted in approximately 40% of collected data meeting strict criteria.

Solar irradiance was measured using a PASCO Wireless Weather Sensor (PS-3209-02) with 300-3000 nm spectral range, 0-2000 W/m^2 measurement range, ±5% accuracy, and 1 W/m^2 resolution. The sensor was co-planar mounted with the test module at 33° tilt for plane-of-array measurements.

Electrical characterization employed a PROVA 210A Solar Module Analyzer performing complete I-V sweeps from short-circuit to open-circuit in under 2 seconds. The instrument provided DC voltage measurement (0-60 V, ±1% accuracy) and current measurement (0-61 A, ±1% accuracy) with minimum 200 data points per curve. The data obtained was saved

directly to a connected computer for further analysis, as shown in **Fig. 1**. The general specifications of the solar module are given in **Table 2**.

Each measurement session included module surface cleaning with deionized water, environmental condition verification, and acquisition of minimum five I-V curves per data point for repeatability confirmation. Quality control required measurement repeatability within 3% standard deviation, environmental stability during acquisition (≤2% irradiance variation, ≤0.5°C temperature variation), and statistical validation with minimum 15 data points per irradiance level. Final measurement uncertainties were ±3% for power and ±2% for efficiency calculations, with 95% confidence intervals reported for all parameters.

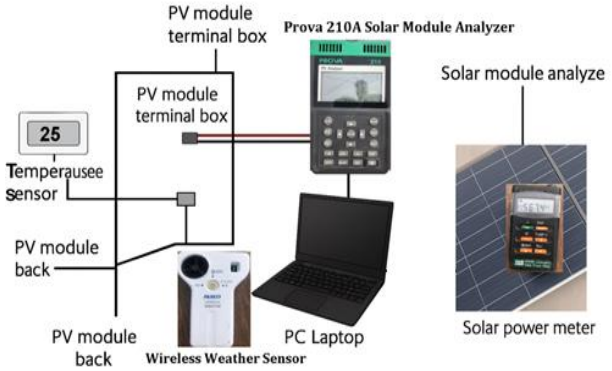

Figure 1. Setup of the experiment.

Table 2. Specification of solar module analyzer (PROVA 210A)

Battery type	Rechargeable, 2500mAh (1.2V) * 8	
AC Adaptor	AC 110V or 220V input DC 12V/1~3A output	
Dimension	257(L) * 155(W) * 57(H) mm	
Weight	1160g	
Operation environment	0 °C - 50 °C , 85% RH (relative humidity)	
Temperature coefficient	0.1% of full scale/ °C (< 18 °C or > 28° C)	
Storage environment	-20° C ~ 60 °C , 75% RH	
Accessories	User manual * 1, AC adaptor*1 Optical USB cable*1 Software CD *1, software manual *1 Kelvin clips(6A max) *1 set	
DC voltage measurements		
Range	**Resolution**	**Accuracy**
0-6	0.001V	±1% ±(1% of V_{open}±9 mV)
6-10 V	0.001V	±1% ±(1% of V_{open}±0.09 V)
10-60 V	0.01 V	±1% ±(1% of V_{open}±0.09 V)
DC current measurements		
Range	**Resolution**	**Accuracy**
0.01-6 A	0.1mA	±1% ±(1% of $I_{short\ n}$±0.09 mA)
0.6-61A	0.1mA	±1% ±(1% of $I_{short\ n}$±0.09 mA)
1-6 A	1mA	±1% ±(1% of $I_{short\ n}$±0.09 mA)

4. THEORETICAL FRAMEWORK

In photovoltaic systems, the portion of solar radiation that is not transformed into electrical output, denoted as (ϕ_{loss}), reflects the total inefficiency in energy conversion. This portion is mathematically defined as the difference between unity and photovoltaic conversion efficiency (η_{pv}), as expressed in Eq. (1) **(Sze and Ng, 2007)**:

$$\phi_{loss} = 1 - \eta_{PV} = 1 - \frac{P_{el}}{GA_{abs}} \quad (1)$$

The result of this equation represents the fraction of solar energy that is lost during the conversion process and not utilized as electrical power. In other words, it quantifies how much of the incoming solar radiation is dissipated in the form of heat, reflection, or other non-electrical losses. This value is dimensionless (a ratio or percentage), and it serves as a key indicator of the overall efficiency limitations of the photovoltaic module.

4.1 Classification of Power Losses in Photovoltaic Modules

Photovoltaic power losses can be classified into five main categories, each reflecting a distinct physical mechanism that limits energy conversion efficiency:
Optical losses (L_1): These occur due to reflection(L_{1R}), transmission (L_{1T}), contact grid shadowing (L_{1sh}), and non-absorptive interactions (L_{1abs}) where photons do not generate charge carriers.
Source-absorber mismatch losses (L_2): Comprised of two primary mechanisms: Sub-bandgap losses (L_{2a}), which result from photons with energies below the bandgap that are not absorbed. Thermalization losses (L_{2b}): due to the excess energy of charge carriers dissipating as heat after photon absorption.
Recombination losses (L_3): Resulting from recombination of electrons and holes, and include: Radiative recombination (L_{3rad}), Non-radiative recombination ($L_{3nrad-J}$), and Shunt-related losses (L_{3sh}).
Voltage losses (L_4): Primarily attributed to the reduction in the open-circuit voltage due to recombination effects.
Thermal losses (L_{therm}): Represent the sum of multiple sub-losses, particularly those not recovered as useful energy, including radiative and non-radiative losses, and are discussed in more detail in subsequent sections.
Radiative recombination losses (L_{3rad}) in silicon occur across the entire wavelength spectrum. However, due to the relatively low efficiency of radiative recombination in silicon, most losses are attributed to non-radiative mechanisms, such as defect- and impurity-assisted recombination **(Richter et al., 2013).** It is generally assumed that radiative recombination contributes only a small portion to the total recombination losses. The total radiative recombination loss ($L_{1R\text{-}tot}$) can be determined using the following Eq. (2) is adapted based on the energy loss classification in silicon photovoltaic modules as discussed by Bruno Lorenzi and further supported by the recombination analysis framework in Richter and Glunz.**:**

$$L_{1R-tot} = L_{1R} + L_{1sh} + L_{3rad} + L_{2a-abs} \quad (2)$$

This equation aggregates the major optical and radiative loss components that directly influence the effective photon conversion, including reflection, shading, radiative

recombination, and sub-bandgap photon loss. Moreover, the total absorption-related losses are calculated using Eq. (3):

$$L_{abs-tot} = L_{1abs} + L_{2a-abs} \tag{3}$$

This equation isolates the absorption-related losses that do not contribute to carrier generation, providing a useful metric for analyzing optical inefficiencies in the solar spectrum.

So ratio thermal power, Based on the classification of internal heat-generating mechanisms, the total recoverable as in Eq. (4) (**Cotfas et al., 2012)**.

$$\xi_u = L_{abs-tot} + L_{2b} + L_{3sh} + L_{3N_{rad-J}} + L_4 \tag{4}$$

This equation calculates the internal thermal losses (ξu) by summing the major contributing loss mechanisms within the solar module. These include absorptive losses, thermalization losses, shunt-related recombination, non-radiative recombination, and voltage losses. Each term in the equation represents a distinct physical process that contributes to heat generation, and their total provides an estimate of the recoverable thermal energy available for potential hybrid PV-T applications, as in Eq. (5).

$$\xi_u = 1-(\eta_{pv} + L_{1R-tot} + L_{1T} + L_{2a-T}) \tag{5}$$

Alternatively, the proportion of internal thermal losses can be expressed as the complement of the useful energy components—namely the electrical efficiency (η_{pv}) and non-thermal optical losses. This formulation offers a simplified energy balance perspective by subtracting known losses and output from the total incident energy.

4.2 Quantum Efficiency

Quantum efficiency, encompassing both external (EQE) and internal (IQE) forms, is used to evaluate how different wavelengths of incident light contribute to optical and electrical losses such as reflection, parasitic absorption, and carrier recombination within the solar cell structure. It represents the ratio between the number of charge carriers collected and the number of incident photons at a specific wavelength. This parameter is critical for understanding the spectral response of photovoltaic materials. In laboratory conditions, the external quantum efficiency (EQE) is calculated as follows as in Eq. (6), By taking advantage of the substitution of Eq. (7) **(Green, 2008; Nelson, 2003)**.

$$\mathrm{EQE}(\lambda) = \frac{\mathrm{I_{out}}(\lambda)}{\mathrm{I_{ph}}(\lambda)} \tag{6}$$

$$I_{ph}(\lambda) = \frac{q\, A_{abs} G(\lambda)}{\frac{hc}{\lambda}} \tag{7}$$

The internal quantum efficiency IQE (λ) accounts for the quantum efficiency excluding losses due to reflection and is expressed as follows as in Eq. (8).

$$IQE(\lambda) = \frac{EQE(\lambda)}{(1-R(\lambda))(1-T(\lambda))} \tag{8}$$

The functions R (λ) and T (λ) denote the wavelength-dependent reflectance and transmittance, respectively of the device, respectively. By applying Eq. (6) and (8), considering T (λ) =0, the result follows. Moreover, approximately 5% of the photons striking the solar cell surface are reflected without being absorbed. With R (λ) typically around 0.05, depending on the panel's design and manufacturing quality, so the internal quantum efficiency becomes as in Eq. (9).

$$IQE(\lambda) = \frac{I_{out}(\lambda)}{I_{ph}(\lambda)} \frac{1}{(1-R(\lambda))} = \frac{I_{out}(\lambda)}{I_{gen}(\lambda)} \quad (9)$$

Where $I_{gen}(\lambda)$ is the generated can be determined as follows as in Eq. (10):

$$I_{gen}(\lambda) = \frac{qG(\lambda)A_{abs}(1-R(\lambda))}{hc/\lambda} \quad (10)$$

Based on Eq. (10), the actual amount of solar energy that enters the solar module, the generated radiation can be calculated as follows as in Eq. (11):

$$G_{gen}(\lambda) = G(\lambda)\big(1 - R(\lambda)\big) \quad (11)$$

4.3 Determination of Losses

The assumptions are:
1. Assume that any photons striking the metallic contact are completely reflected
2. All photons are emitted
3. T(λ) = 0, and thus $L_{1T} = L_{2a-T} = 0$

Losses and measured quantities as follows as in Eq. (12) **(Lorenzi et al., 2018).**

$$L_{1R-tot} = L_{1R} + L_{1sh} + L_{3rad} + L_{2a-R} = \frac{\int G(\lambda)R(\lambda)\, d\lambda}{\int G(\lambda) d\lambda} \quad (12)$$

L_{1R-tot} is given by

$$L_{1R-tot}(\lambda) \propto R(\lambda) \quad (13)$$

By employing Eq. (12) for $L_{1R\text{-}totL}$ and Eq. (11) for $G_{gen}(\lambda)$, the remaining losses can be determined. The sub-bandgap component L_{2a}, which contributes to the total absorption loss $L_{abs\text{-}tot,}$ is expressed as follows as in Eq. (14).

$$L_{2a-abs}(\lambda) = \frac{G_{gen}(\lambda)}{G(\lambda)} * H\big(\lambda - \lambda_g\big) \quad (14)$$

Here, H (z) represents the Heaviside step function, defined as:

H(z)= (1 or 0), $\begin{cases} 1 & \text{for } z > 0 \\ 0 & \text{otherwise} \end{cases}$

($\lambda_{g)}$ is given by ($\lambda_g = h_c/E_g$)

Where E_g is the energy bandgap of the absorbing material. The value of (L_{2b}) is then determined as follows as in Eq. (15).

$$L_{2b}(\lambda) = \frac{G_{gen}(\lambda)\, IQE(\lambda)}{G(\lambda)} \left(\frac{\lambda_g}{\lambda} - 1\right) H(\lambda_g - \lambda) \quad (15)$$

(L_4) losses accounting as follows as in Eq. (16).

$$L_4(\lambda) = L_{4carnot} + L_{4boltz} + L_{4Nrad-V} + L_{4s} = \frac{G_{gen}(\lambda) IQE(\lambda)}{G(\lambda)} \left(1 - \frac{qV_{mp}}{E_g}\right) H(\lambda_g) - \lambda) \quad (16)$$

Carnot loss ($L_{4carnot}$) derived by Eq. (16A.1).

$$V_{4carnot} \approx \frac{E_g}{q} \frac{T_c}{T_s} \quad (16A.1)$$

Where (T_c) denotes the temperature of the solar cell, while (T_s) refers to the Sun's temperature.
The voltage drop is calculated as in Eq. (16A.2).

$$V_{4bolts} \approx \frac{k_B}{q} \ln\left(\frac{\Omega_{emit}}{\Omega_{abs}}\right) \quad (16A.2)$$

Where (k_B) represents the Boltzmann constant, (Ω_{emit}) and (Ω_{abs}) correspond to the solid angles of emission and absorption, respectively.
The overall voltage reduction caused by (L_4) is given as follows as in Eq. (16A.3).

$$V_4 = \frac{E_g}{q} - V_{mp} = V_{carnot} + V_{4boltz} + V_{4Nrad-V} - V_{4s} \quad (16A.3)$$

While (V_{mp}) is measured, the combined value of the two unknown voltage drops is expressed as follows as in Eq. (16A.4).

$$V_{4Nrad-V} + V_{4s} = \frac{E_g}{q} - V_{mp} - V_{4carnot} - V_{aboltz} \quad (16A.4)$$

Using Eq. (16), the total value of (L_4) is determined, while Eq. (16A.1, 16A.2, and 16A.4), and provide the ratio between the various components, allowing the identification of the loss components ($L_{4carnot}$, L_{4boltz}, and $L_{4Nrad-V}$ + L_{4s}). Notably, (V_{4s}) can also be obtained by evaluating the series resistance of the solar cell as follows as in Eq. (16A.5).

$$V_{4s} = R_s I_{mp} \quad (16A.5)$$

Where R_s denotes the resistance went be measured by different methods **(Outes et al., 2020)**, and I_{mp} is the maximum solar module current. Thermal losses L_{therm}, computable as in Eq. (17)

$$L_{therm}(\lambda) = L_{3Nrad-J}(\lambda) + L_{1abs}(\lambda) + L_{3sh}(\lambda) = \frac{G_{gen}(\lambda)[1-IQE(\lambda)]}{G(\lambda)} \quad (17)$$

Eq. (17) quantifies the thermal power generated within the solar module, as a result of optical and recombination losses, and serves as the physical representation of heat generation.
Using both Eqs. (3) and (4), in combination with Eq. (15-17) one can determine (ξ_u) as in Eq. (18).

$$\xi_u(\lambda) = L_{2a-abs}(\lambda) + L_{2b}(\lambda) + L_4(\lambda) + L_{therm}(\lambda) \quad (18)$$

To further quantify the internal optical and thermal losses in photovoltaic modules, additional calculations were performed based on external quantum efficiency (EQE), internal quantum efficiency (IQE), and the optical absorption properties of the device. These relationships help in understanding how much of the incident photon energy is effectively utilized versus lost through various mechanisms such as reflection, non-absorbed photons, and recombination processes. The following Eqs. (19–22) define these parameters **(Sze and Ng, 2007)**.

$$R_{rad} = RP_o \left[\exp\left(\frac{eV}{k_B T}\right) - 1\right] \quad (19)$$

$$RR_o = \frac{2\pi}{c^2 h^3} \int_{E_g}^{\infty} \frac{E^2 dE}{\exp\left[E/k_B T\right] - 1} \quad (20)$$

$$L_{3rad} = \frac{I_{rad}}{I_{gen}} = \frac{qR_{rad}A_{abs}}{I_{gen}} \quad (21)$$

$$\mathrm{L_{3rad}}(\lambda) = \frac{\mathrm{hc\ R_{rad}}}{\lambda\ \mathrm{G_{gen}}(\lambda)} \quad (22)$$

These equations serve as a foundation for analyzing the spectral performance and internal losses of the PV module, allowing for a more accurate evaluation of energy conversion efficiency under varying irradiation conditions. The outcomes derived from these expressions are further validated through experimental measurements, as discussed in the following sections.

5. RESULTS AND DISCUSSION

The present work involved practical measurements on a multicrystalline silicon solar panel under controlled conditions, as illustrated in **Fig. 1** which shows the experimental setup. Data collection included open-circuit voltage, short-circuit current, and maximum power output across varying irradiance levels while maintaining module temperature at 25°C. This temperature was selected to comply with Standard Test Conditions (STC: 1000 W/m^2, 25°C, AM 1.5 spectrum) established by IEC 61215, enabling direct comparison with manufacturer specifications and ensuring reproducible results for thermal loss quantification. Solar irradiance was maintained at discrete levels of 250, 500, 750, and 1000 W/m^2 through strategic timing and atmospheric condition selection, as presented in **Table 3**. The data in this table reveals several critical performance trends that directly impact thermal loss mechanisms.
Maximum power (P_{max}) exhibits an approximately linear relationship with irradiance, increasing from 70.9 W at 250 W/m^2 to 324.0 W at 1000 W/m^2. This near-linear scaling indicates consistent photon-to-electron conversion efficiency across the tested irradiance

range, with the proportionality constant reflecting the module's fundamental conversion characteristics. Short-circuit current (I_{sc}) demonstrates strong irradiance dependence, rising from 2.25 A to 9.14 A across the measurement range. This behavior aligns with photovoltaic theory, where I_{sc} is directly proportional to photon flux density, confirming that current generation scales effectively with available solar energy. The open-circuit voltage (V_{oc}) exhibits minimal variation (44.2 V to 45.8 V), consistent with its logarithmic dependence on irradiance and temperature stability at 25°C. At the maximum power point, voltage (V_{max}) shows modest increases from 37.5 V to 40.9 V, while current (I_{max}) increases substantially from 1.89 A to 7.92 A. This demonstrates that power enhancement with increasing irradiance is primarily driven by current rather than voltage changes, a characteristic behavior of silicon photovoltaic devices under constant temperature conditions.

The Fill Factor (FF) behavior reveals important insights into module performance optimization. The peak FF value of 0.812 occurs at 500 W/m^2, declining to 0.722 at 1000 W/m^2. This non-monotonic trend indicates that optimal electrical performance occurs at moderate irradiance levels, where the balance between photocurrent generation and internal loss mechanisms is most favorable. Module efficiency (η) exhibits a similar pattern, achieving maximum value of 18.1% at 500 W/m^2 before decreasing to 16.7% at 1000 W/m^2. This efficiency-irradiance relationship appears counterintuitive but reflects the complex interplay between beneficial and detrimental effects of increased photon flux. While higher irradiance generates more photocurrent, it simultaneously increases internal heat generation, leading to enhanced recombination rates and reduced voltage performance despite constant module temperature. The observed efficiency reduction at high irradiance, even under temperature-controlled conditions, indicates that thermal loss mechanisms become increasingly dominant as photon flux increases. This finding has significant implications for photovoltaic system design in high-irradiance environments, such as the arid climate conditions of Iraq, where peak solar irradiance can exceed 1000 W/m^2.

Table 3. Multicrystalline solar module parameters with different solar radiations and solar module operating temperature 25(° C).

G (W/m^2)	I_{sc} (A)	V_{oc} (V)	I_{max} (A)	V_{max} (V)	P_{max} (W)	FF	η
250	2.25	44.20	1.890	37.50	70.9	0.713	14.6
500	4.73	45.60	4.500	38.98	175.3	0.812	18.1
750	7.18	46.00	6.32	39.56	250.1	0.759	17.2
1000	9.14	45.80	7.92	40.91	324.0	0.722	16.7

Table 4 presents the quantified loss components across the irradiance range, revealing the fundamental energy conversion pathways within the multicrystalline silicon module. **Fig. 2** provides a visual representation of these computed losses for the multicrystalline solar module under 1000 W/m^2 solar irradiance. Total optical reflection losses ($L_{1R\text{-}tot}$) remain constant at approximately 40% across all irradiance levels, as expected for surface-dependent phenomena. This consistency validates the assumption that reflection losses are primarily determined by the module's anti-reflective coating properties and surface texturing rather than incident photon flux density.

Radiative recombination losses (L_{3rad}) are minimal, ranging from 0.12% to 0.44%, confirming that silicon's indirect bandgap nature results in predominantly non-radiative recombination mechanisms. Sub-bandgap absorption losses ($L_{2a\text{-}abs}$) remain negligible

across the measurement range, indicating efficient photon utilization within the silicon's spectral response window.

Thermalization losses (L_{2b}) increase with decreasing irradiance, from 0.05% at 1000 W/m^2 to 1.32% at 250 W/m^2. This trend reflects the changing photon energy distribution and absorption characteristics under varying flux conditions.

Thermal losses (L_{therm}) exhibit a strong irradiance dependence, increasing from 10.33% at 250 W/m^2 to 19.02% at 1000 W/m^2. This substantial increase demonstrates that higher photon flux densities generate proportionally more internal heat through non-radiative recombination, optical absorption without carrier generation, and other loss mechanisms. The nearly linear relationship between thermal losses and irradiance provides critical data for hybrid photovoltaic-thermal system design.

Voltage losses (L_4) remain relatively stable between 15.60% and 18.07%, indicating consistent thermodynamic limitations across the irradiance range. The recoverable thermal energy fraction (ξ_u) varies from 29.72% to 35.06%, representing substantial energy quantities available for thermal recovery applications.

Total losses range from 70.61% to 74.93%, confirming that the majority of incident solar energy is converted to forms other than useful electrical output. This energy balance provides fundamental insights into the theoretical limits and practical optimization strategies for multicrystalline silicon photovoltaic systems. **Fig. 3 (a, b, c)** illustrates the computed losses for the multicrystalline solar module under various solar irradiance levels of 250, 500, and 750 W/m^2, respectively, providing a comprehensive view of loss distribution across different operating conditions.

Table 4. Values of computed losses in percentage (%).

G (w/m^2)	$L_{1R\text{-}tot}$ (%)	L_{3rad} (%)	$L_{2a\text{-}abs}$ (%)	L_{2b} (%)	L_{therm} (%)	L_4 (%)	$\xi_u(\lambda)$ (%)	Total (%)
1000	40	0.12	0.0	0.05	19.02	15.60	34.68	74.93
750	40	0.13	0.0	0.28	17.03	17.74	35.06	75.33
500	40	0.24	0.0	0.79	14.13	18.05	32.98	73.45
250	40	0.44	0.0	1.32	10.33	18.07	29.72	70.61

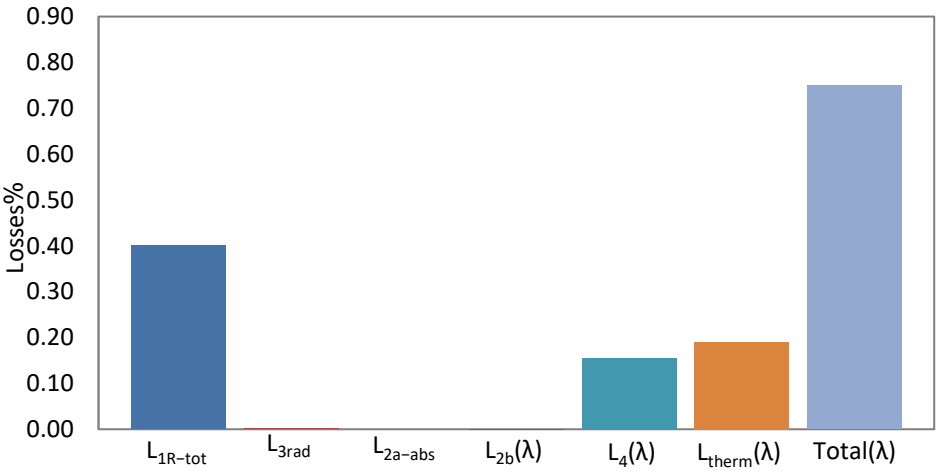

Figure 2. Computed losses of a multicrystalline solar module under solar irradiance of 1000 W/m^2.

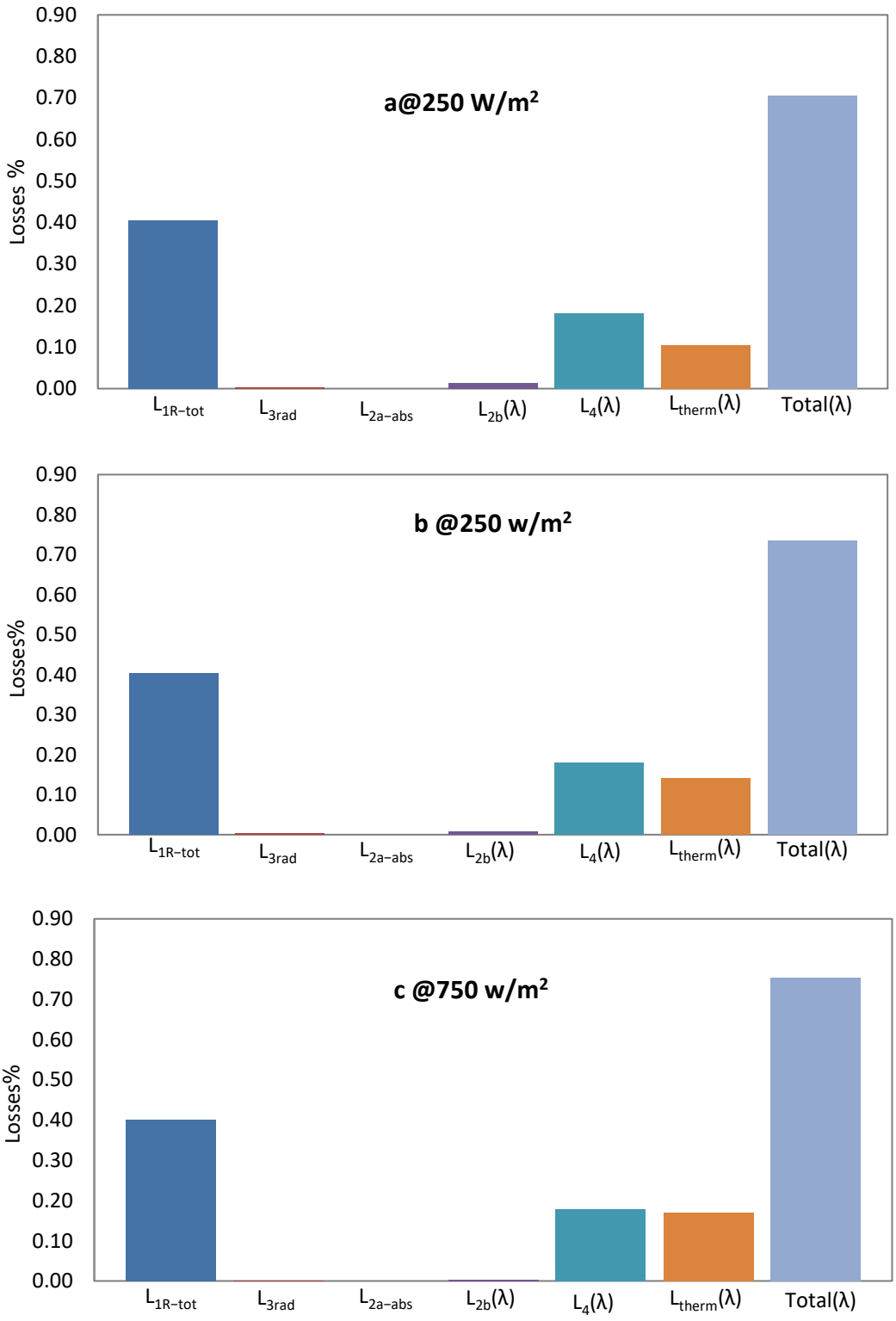

Figure 3. Computed losses of a multicrystalline solar module under solar irradiance of (a@ 250, b@500, c@750) W/m^2.

Table 5 compares the experimental results with theoretical calculations from **(Lorenzi et al., 2018)** for multicrystalline silicon under identical conditions (1000 W/m^2, 25°C. Losses view of solar module structure where thermal losses are highlighted within red-bordered

squares, providing the theoretical framework for this comparison. The comparison reveals both agreements and discrepancies that provide insights into the experimental validation of thermal loss models. The measured total reflection losses (40%) significantly exceed the theoretical value (16.29%), suggesting that the test module's surface characteristics, age, or soiling conditions result in higher optical losses than idealized model assumptions. This difference emphasizes the importance of real-world validation for theoretical predictions. Thermal losses show reasonable agreement (19.02% experimental vs. 9.39% theoretical), with the experimental values being higher. This difference may reflect additional loss mechanisms not fully captured in the theoretical framework, including temperature non-uniformities, partial shading effects, or degradation-related losses in the aged module. The overall error margins, ranging from -34% to +145% for individual components, highlight the challenges in experimentally validating complex loss mechanisms. However, the total loss comparison shows better agreement (-14.0% error), suggesting that while individual loss components may vary significantly, the overall energy balance provides more reliable validation.

Table 5. A comparison between the experimental calculations and Bruno Lorenzi's calculations at 1000 W/m^2 irradiance, with a margin of error (%).

G (w/m^2)	**Research**	**$L_{1R\text{-}tot}$** (%)	**L_{3rad}** (%)	**$L_{2a\text{-}abs}$** (%)	**L_{2b}** (%)	**L_{therm}** (%)	**L_4** (%)	**Total** (%)
1000	**Present work**	40	0.12	0	0.05	19.02	15.60	74.93
	(Acciarri et al., 2018)	16.29	1.48	14.63	21.83	9.39	23.52	87.16
	Error (%)	+145.6	−91.9	−100.0	−99.8	+102.5	−33.6	−14.0

Fig. 4 demonstrates that the recoverable thermal energy fraction (ξ_u) is distributed relatively uniformly across the solar spectrum rather than concentrated in infrared wavelengths. This spectral distribution has critical implications for thermal recovery system design, indicating that effective heat extraction strategies should accommodate the entire solar spectrum rather than targeting specific wavelength ranges. The uniform distribution contradicts common assumptions that thermal losses are primarily infrared-related and suggests that spectrum-splitting approaches for hybrid photovoltaic-thermal systems should consider broadband thermal extraction mechanisms. This finding supports the development of full-spectrum thermal management solutions optimized for the specific spectral characteristics of multicrystalline silicon modules.

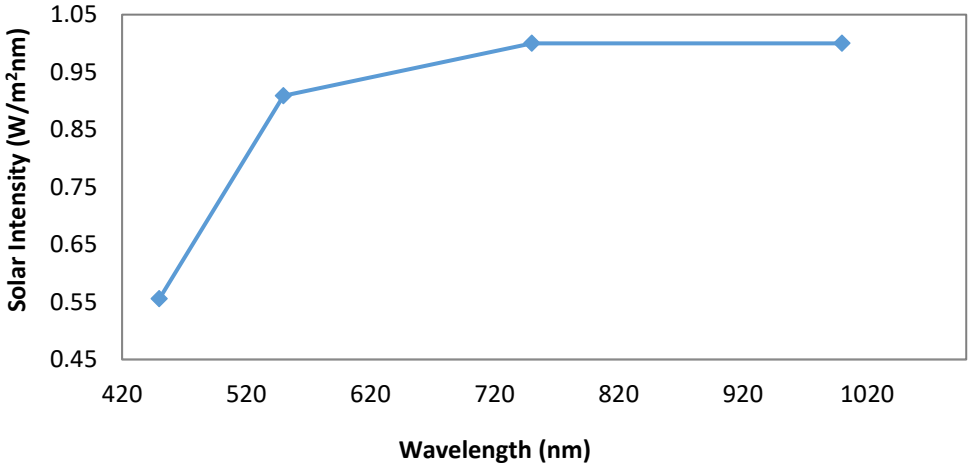

Figure 4. Spectral dependency of (ξ_u) multicrystalline solar module.

Tables 6 and 7 present external quantum efficiency (EQE) and internal quantum efficiency (IQE) values at representative wavelengths across the irradiance range, while **Figs. 5 and 6** show the relationships between EQE and IQE with irradiation at various wavelengths, respectively. The measurement methodology employed standard photovoltaic characterization techniques, with wavelength-specific responses derived from spectral response measurements rather than monochromatic irradiance sources. Both EQE and IQE show slight increases with decreasing irradiance, ranging from 0.58-0.65% at 1000 W/m^2 to 1.28-1.43% at 250 W/m^2 depending on wavelength. This trend reflects improved charge carrier collection efficiency under reduced photon flux conditions, where recombination rates are lower and carrier transport is more effective. The wavelength dependence follows expected patterns for multicrystalline silicon, with optimal response in the visible spectrum and reduced efficiency at longer wavelengths due to decreased absorption coefficients and increased recombination losses.

The experimental results provide specific insights for photovoltaic applications in Iraq's arid climate, where solar irradiance frequently exceeds 1000 W/m^2 and ambient temperatures can reach 45-50°C. The observed efficiency reduction at high irradiance, even under controlled temperature conditions, suggests that thermal management becomes increasingly critical as irradiance levels rise. The substantial recoverable thermal energy (30-35% of incident solar energy) represents a significant opportunity for hybrid system development in high-irradiance environments. The uniform spectral distribution of this thermal energy indicates that cooling strategies should address the entire solar spectrum rather than targeted wavelength ranges.

These findings support the development of integrated photovoltaic-thermal systems optimized for arid climates, where abundant solar resources enable both electrical generation and thermal energy recovery. The quantified loss mechanisms provide the fundamental data necessary for designing effective hybrid systems that maximize total energy utilization under extreme environmental conditions.

Table 6. External quantum efficiency values at varying wavelengths.

EQE 250) W/m^2) λ 450(nm)%	**EQE 500(W/m^2) λ 550(nm)%**	**EQE 750(W/m^2) λ 750(nm)%**	**EQE 1000(W/m^2) λ 1000(nm)%**
1.28	1.05	0.77	0.58
1.35	1.10	0.81	0.61
1.36	1.11	0.82	0.61
1.30	1.06	0.78	0.59

Table 7. Internal quantum efficiency values at different wavelengths.

IQE 250(W/m^2) λ 450(nm) %	**IQE 500(W/m^2) λ 550(nm)%**	**IQE 750(W/m^2) λ 750(nm)%**	**IQE 1000(W/m^2) λ 1000(nm)%**
1.35	1.10	0.81	0.61
1.42	1.16	0.85	0.64
1.43	1.17	0.86	0.65
1.37	1.12	0.82	0.62

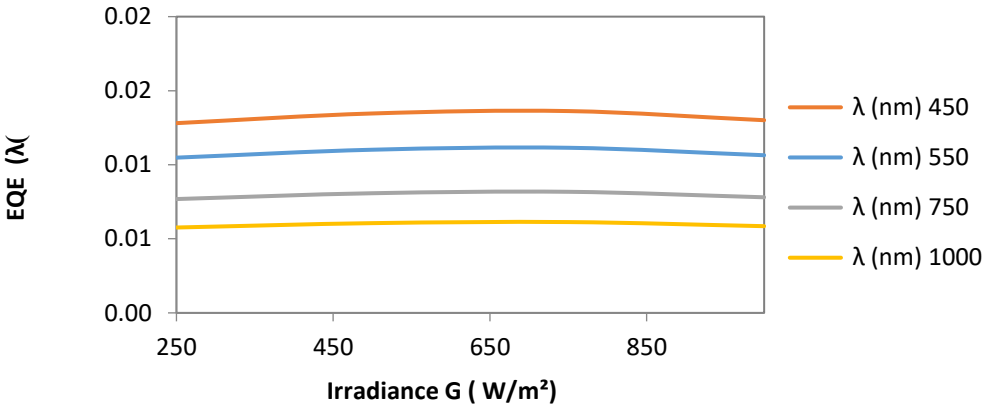

Figure 5. The external quantum efficiency with irradiation at various wave lengths.

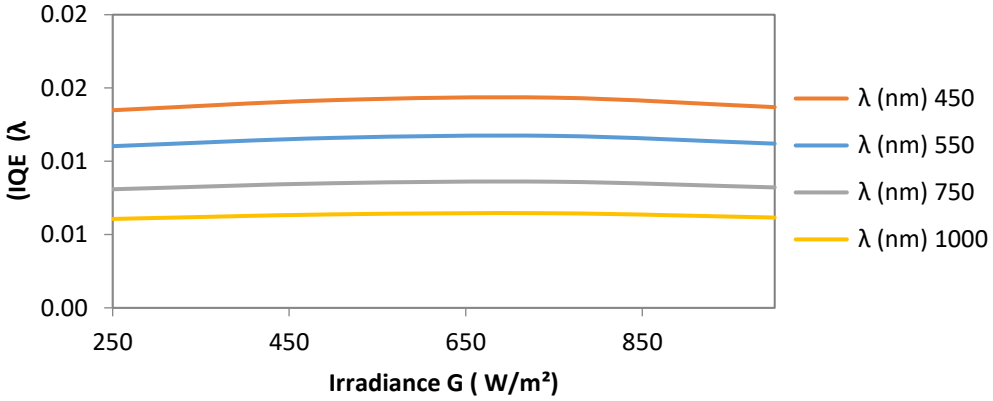

Figure 6. The internal quantum efficiency with irradiation at various wave lengths.

6. CONCLUSIONS

This study provides the first comprehensive analysis of thermal loss mechanisms in multicrystalline silicon photovoltaic modules under Iraqi climatic conditions. Key findings include:

1. Irradiance-Dependent Thermal Losses: Thermal losses increase from 10.33% to 19.02% as irradiance increases from 250 to 1000 W/m^2, indicating significant heat generation potential for hybrid applications.
2. Recoverable Thermal Energy: The (ξ_u) values (29.72-35.06%) represent substantial recoverable thermal energy, distributed across the complete solar spectrum rather than concentrated in infrared wavelengths.
3. Efficiency-Irradiance Relationship: The observed efficiency decrease with increasing irradiance (18.1% to 16.7%) demonstrates the dominance of thermal losses over optical gains in high-irradiance conditions typical of arid climates.

Unlike prior studies that treat optical and thermal losses in isolation, this work presents an integrated approach that quantifies the extractable thermal energy (ξ_u) and its potential role in hybrid PV-thermal systems. The outcomes are particularly relevant to regions with high solar potential, such as Iraq, where ambient conditions can be leveraged for dual electrical and thermal energy harvesting. Future research should explore dynamic heat extraction mechanisms, advanced materials, and real-time thermal management strategies to further enhance PV performance and sustainability in arid and semi-arid climates.

Nomenclature

Symbol	Description	Symbol	Description
A_{abs}	Absorber area of the solar module (m^2)	L_{1R}	Reflection losses (%)
EQE(λ)	External Quantum Efficiency (%)	L_{1R-tot}	Total optical reflection losses (%)
FF	Fill Factor	L_{1sh}	Shadowing losses due to front contacts (%)
G	Solar irradiance (W/m^2)	L_{1T}	Transmission losses (%)
$G_{gen(\lambda)}$	Photogeneration power density (W/m^2)	L_{1abs}	Optical absorption losses with no carrier generation (%)
$I_{out(\lambda)}$	Output photocurrent at wavelength λ (A)	L_{2a-abs}	Sub-bandgap absorption losses (%)
$I_{ph(\lambda)}$	Incident photon current at wavelength λ (A)	L_{2a-T}	Thermalization component of sub-bandgap losses (%)
I_{sc}	Short-circuit current (A)	L_{2b}	Carrier thermalization losses (%)
I_m	Current at maximum power point (A)	P_{el}	Electrical output power (W)
$L_{3nrad-J}$	Non-radiative recombination losses (%)	P_m	Maximum power output (W)
L_{3rad}	Radiative recombination losses (%)	T	Temperature (C° or K)
L_{3sh}	Recombination via shunt paths (%)	V_{oc}	Open-circuit voltage (V)
L_4	Voltage loss due to recombination (%)	V_m	Voltage at maximum power point (V)
$L_{abs-tot}$	Total absorption-related losses (%)	η_{PV}	Photovoltaic conversion efficiency (%)
L_{therm}	Thermal losses (%)	$\xi_{u(\lambda)}$	Recoverable thermal energy fraction (%)
IQE(λ)	Internal Quantum Efficiency (%)	Φ_{loss}	Total energy losses (fraction of input solar power not converted) (%)

Credit Authorship Contribution Statement

Hassanein Saady Hussein: Writing -original draft, review and editing, research and Methodology. Adawiya Ali: Supervision and Proofreading.

Declaration of Competing Interest

The authors declare that they have no known competing financial interests or personal relationships that could have appeared to influence the work reported in this paper.

REFERENCES

Aghaei, M., Kumar, N.M., Eskandari, A., Ahmed, H., Vidal de Oliveira, A.K., and Chopra, S.S., 2020. Solar PV systems design and monitoring. In: *Photovoltaic Solar Energy Conversion*. Academic Press, pp. 117–145. https://doi.org/10.1016/B978-0-12-819610-6.00005-3

Arifin, Z., Suyitno, S., Tjahjana, D.D., Juwana, W.E., and Putra, M.R., 2020. The effect of heat sink properties on solar cell cooling systems. *Applied Sciences*, 10(21), P. 7919. https://doi.org/10.3390/app10217919

Asif, M.H., Zhongfu, T., Ahmad, B., Irfan, M., Razzaq, A., and Ameer, W., 2023. Influencing factors of consumers' buying intention of solar energy: A structural equation modeling approach. *Environmental Science and Pollution Research*, 30(11). https://doi.org/10.1007/s11356-022-23627-8

Aslam, A., Ahmed, N., Qureshi, S.A., Assadi, M., and Ahmed, N., 2022. Advances in solar PV systems; A comprehensive review of PV performance, influencing factors, and mitigation techniques. *Energies*, 15(20), P. 7595. https://doi.org/10.3390/en15207595

Barron-Gafford, G.A., Minor, R.L., Allen, N.A., Cronin, A.D., Brooks, A.E., and Pavao-Zuckerman, M.A., 2016. The photovoltaic heat island effect: Larger solar power plants increase local temperatures. *Scientific Reports*, 6(1), P. 35070. https://doi.org/10.1038/srep35070

Bhore, C.V., Andhare, A.B., Padole, P.M., Loyte, A., Vincent, J.S., Devarajan, Y., and Vellaiyan, S., 2023. Experimental investigation on minimizing degradation of solar energy generation for photovoltaic module by modified damping systems. *Solar Energy*, 250, pp. 194–208. https://doi.org/10.1016/j.solener.2022.10.031

Cotfas, D.T., Cotfas, P.A., Ursutiu, D., and Samoila, C., 2012. In: *2012 13th International Conference on Optimization of Electrical and Electronic Equipment (OPTIM)*. IEEE, pp. 966–972. ISBN 978-1-4673-1653-8. https://lib.ugent.be/catalog/ebk01:3420000000000684

Dupre, O., Vaillon, R., and Green, M.A., 2016. Recombination mechanisms in photovoltaic devices. *Solar Energy*, 140, pp. 73–85. https://doi.org/10.1016/j.solener.2016.10.019

Fang, S., Lyu, X., Tong, T., Lim, A.I., Li, T., Bao, J., and Hu, Y.H., 2023. Turning dead leaves into an active multifunctional material as evaporator, photocatalyst, and bioplastic. *Nature Communications*, 14(1), P. 1203. https://doi.org/10.1038/s41467-023-36878-3

Green, M. A., 2006. Third Generation Photovoltaics: Advanced Solar Energy Conversion, *Springer*. https://doi.org/10.1007/3-540-28829-9

Hashim, E.T. and Abbood, A.A., 2016. Temperature effect on power drop of different photovoltaic module. *Journal of Engineering*, 22(5), pp. 126–143. https://doi.org/10.31026/j.eng.2016.05.09

Hashim, E.T. and Talib, Z.R., 2018. Study of the performance of five parameter model for monocrystalline silicon photovoltaic module using a reference data. *FME Transactions*, 46, pp. 585–594. https://doi.org/10.5897/AJEST2018.2566

Hashim, E.T. and Talib, Z.R., 2018. Modeling and simulation of solar module performance using five parameters model by using MATLAB in Baghdad City. *Journal of Engineering*, 24(10), pp. 15–31. https://doi.org/10.31026/j.eng.2018.10.02

Hashim, E.T., 2016. Determination of Mono-Crystalline Silicon photovoltaic module parameters using three different methods. *Journal of Engineering*, 22(7), pp. 92–107. https://doi.org/10.31026/j.eng.2016.07.06

Hernandez-Callejo, L., Gallardo-Saavedra, S., and Alonso-Gomez, V., 2019. A review of photovoltaic systems: Design, operation and maintenance. *Solar Energy*, 188, pp. 426–440. https://doi.org/10.1016/j.solener.2019.06.017

Hibberd, C., Plyta, F., Monokroussos, C., Bliss, M., Betts, T., & Gottschalg, R., 2011. Voltage-dependent quantum efficiency measurements of amorphous silicon multi-junction mini-modules. *Solar Energy Materials and Solar Cells*, 95, pp. 123–126. https://doi.org/10.1016/j.solmat.2010.04.125

Kadia, N.J., Hashim, E.T., and Abdullah, I.B., 2022. Performance of different photovoltaic technologies for Amorphous Silicon (A-Si) and Copper Indium Gallium Di Selenide (CIGS) photovoltaic modules. *Journal of Engineering and Sustainable Development*, 26(1), pp. 95–105. https://doi.org/10.31272/jeasd.26.1.10

Katee, N.S., Abdullah, I.B., and Hashim, E.T., 2022. Extracting four solar model electrical parameters of Mono-Crystalline Silicon (mc-Si) and Thin Film (CIGS) solar modules using different methods. *Journal of Engineering*, 27(4), pp. 16–32. https://doi.org/10.31026/j.eng.2021.04.02

Kraemer, D., Hu, L., Muto, A., Chen, X., Chen, G., and Chiesa, M., 2008. *Applied Physics Letters*, 92(24), P. 243503. https://doi.org/10.1063/1.2946676

Lipiński, W., Abbasi-Shavazi, E., Chen, J., Coventry, J., Hangi, M., Iyer, S., Kumar, A., Li, L., Li, S., Pye, J., and Torres, J.F., 2020. Progress in heat transfer research for high-temperature solar thermal applications. *Applied Thermal Engineering*, 184, P. 116137. https://doi.org/10.1016/j.applthermaleng.2020.116137

Lorenzi, B., Acciarri, M., & Narducci, D., 2018. Experimental determination of power losses and heat generation in solar cells for photovoltaic–thermal applications. *Journal of Materials Engineering and Performance*, 27(12), pp. 6291–6298. https://doi.org/10.1007/s11665-018-3604-3

Ma, Y., Yang, K., Shi, X., Ding, W., Ni, L., and Jin, L., 2021. Design of cold chain container energy storage and conversion system based on modularization. In: *2021 IEEE 5th Conference on Energy Internet and Energy System Integration (EI2)*, pp. 698–703. IEEE. https://ieeexplore.ieee.org/document/9713245

Mesquita, I., Andrade, L., and Mendes, A., 2019. Temperature impact on perovskite solar cells under operation. *Chemsuschem*, 12(10), pp. 2186–2194. https://doi.org/10.1002/cssc.201802899

Mizoshiri, M., Mikami, M., and Ozaki, K., 2012. Thermal–photovoltaic hybrid solar generator using thin-film thermoelectric modules. *Japanese Journal of Applied Physics*, 51(6S), P. 06FL07. ISSN 0021-4922. https://doi.org/10.1143/JJAP.51.06FL07

Mohammed, S.A. and Hashim, E.T., 2019. Designing a maximum power point tracking system for a Monocrystalline silicon solar module using the Arduino microcontroller and synchronous buck converter. *FME Transactions*, 47, pp. 524–533. https://doi.org/10.5937/fmet1903524M

Nelson, J., 2003. *The Physics of Solar Cells*, Imperial College Press, London. https://doi.org/10.1142/p276

Nkounga, W.M., Ndiaye, M.F., Ndiaye, M.L., Grandvaux, F., Tabourot, L., and Conde, M., 2021. Sizing optimization of a charging station based on the multi-scale current profile and particle swarm optimization: application to power-assisted bikes. In: *2021 Sixteenth International Conference on Ecological Vehicles and Renewable Energies (EVER)*, pp. 1–12. IEEE. https://univ-smb.hal.science/hal-03457476/document

Outes, C., Fernández, E.F., Seoane, N., Almonacid, F., and García-Loureiro, A.J., 2020. Numerical optimisation and recombination effects on the vertical-tunnel-junction (VTJ) GaAs solar cell up to 10,000 suns. *Solar Energy*, 203, pp. 136–144. https://doi.org/10.1016/j.solener.2020.04.029.

Richter, A., Hermle, M., and Glunz, S.W., 2013. Reassessment of the limiting efficiency for crystalline silicon solar cells. *IEEE Journal of Photovoltaics*, 3(4), pp. 1184–1191. https://doi.org/10.1109/JPHOTOV.2013.2270351

Sarath, K.P., Osman, M.F., Mukesh, R., Manu, K.V., and Deepu, M., 2023. A review of the recent advances in the heat transfer physics in latent heat storage systems. *Thermal Science and Engineering Progress*, 12, P. 101886. https://doi.org/10.1016/j.tsep.2023.101886

Sharma, S.K., Navadeep, S., Francesco, R., and Nguyen, T.T., 2019. Nanoparticles-based magnetic and photo induced hyperthermia for cancer treatment. *Nano Today*, 29, P. 100795. https://doi.org/10.1016/j.nantod.2019.100795

Sun, C., Zou, Y., Qin, C., Zhang, B., and Wu, X., 2022. Temperature effect of photovoltaic cells: A review. *Advanced Composites and Hybrid Materials*, 5(4), pp. 2675–2699. https://doi.org/10.1007/s42114-022-00533-z

Sze, S.M. and Ng, K.K., 2007. *Physics of Semiconductor Devices*. 3rd ed. Hoboken, NJ: John Wiley & Sons. https://doi.org/10.1002/9780470068328

Vorobiev,Y., González-Hernández, J., Vorobiev, P., and Bulat, L., 2005. *Solar Energy*, 80, pp. 170–176. ISSN 0038-092X. https://doi.org/10.1016/j.solener.2005.04.022

Wei, J., Wang, Q., Huo, J., Gao, F., Gan, Z., Zhao, Q., and Li, H., 2021. Mechanisms and suppression of photoinduced degradation in perovskite solar cells. *Advanced Energy Materials*, 11(3), P. 2002326. https://doi.org/10.1002/aenm.202002326

Zhou, J., Yi, Q., Wang, Y., and Ye, Z., 2015. Temperature Distribution of Photovoltaic Module Based on Finite Element Simulation. *Solar Energy*, 111, pp. 97–103. https://doi.org/10.1016/j.solener.2014.10.040

دراسة توليد الحرارة وفقدان الطاقة في وحدة الخلايا الشمسية المصنوعة من السيليكون متعدد البلورات

حسين سعدي حسين *، عدوية علي حمزة

قسم هندسة الطاقة، كلية الهندسة، جامعة بغداد، بغداد، العراق

الخلاصة

تحول وحدات الخلايا الشمسية (Photovoltaic modules) جزءًا فقط من الطاقة الشمسية الساقطة إلى كهرباء، بينما يُبدد الباقي على شكل حرارة عبر آليات فقد مختلفة. تهدف هذه الدراسة إلى محاولة تحديد كمية الطاقة الحرارية القابلة للاسترجاع من وحدات السيليكون متعدد البلورات تحت ظروف إشعاع مختلفة في المناخات الجافة. أُجريت القياسات التجريبية على مدى ستة أشهر في بغداد، العراق. وتمت معالجة البيانات للحفاظ على درجة حرارة اللوح عند 25°م عبر أربعة مستويات إشعاعية (250، 500، 750، 1000 واط/م² .(أظهرت النتائج أن الخسائر الحرارية تزداد من 10.33٪ إلى 19.02٪ مع ارتفاع الإشعاع، في حين تتراوح نسبة الطاقة الحرارية القابلة للاسترجاع (ξu) بين 29.72٪ و35.06٪. انخفضت كفاءة اللوح من 18.1٪ عند 500 واط/م² إلى 16.7٪ عند 1000 واط/م²، مما يعكس هيمنة الخسائر الحرارية على المكاسب الضوئية. أظهر التحليل الطيفي أن الطاقة الحرارية القابلة للاسترجاع موزعة بشكل موحد على كامل الطيف الشمسي، وليست مركزة في منطقة الأشعة تحت الحمراء توفر الخسائر الحرارية المحددة في هذه الدراسة بيانات أساسية لتطوير أنظمة هجينة فوتوفولطية–حرارية (PV/T) مصممة خصيصًا لظروف الإشعاع العالي في المناطق الجافة، مما يدعم تقدم الطاقة المتجددة في الأماكن التي تتوفر فيها موارد شمسية وفيرة لتمكين الجمع بين إنتاج الكهرباء والطاقة الحرارية.

الكلمات المفتاحية :السيليكون متعدد البلورات، الخسائر الحرارية، الكفاءة الكمومية، الأنظمة الهجينة الفوتوفولطية–الحرارية، الإشعاع الشمسي، المناخ الجاف.